ROYAL SOCIETY
OF CHEMISTRY

PAPER

Check for updates

Tailoring an efficient computational methodology for studying ligand interactions with heavy radiometals in solution: the case of radium†

Hamissou Mohaman, [ID] [ab] Steffen Happel,[c] Gilles Montavon[b] and
Nicolas Galland [ID] *[a]

The availability of metallic radioelements, with only short-lived isotopes, at trace quantities, does not allow simple, straightforward evaluation of their chemical properties, although they represent societal issues of primary importance (environmental contamination, uses in nuclear medicine, *etc.*). A strategy is presented to establish a cost-effective computational methodology that is radiometal-specific and accurate to supplement the limited experimental data with a focus on complexation properties. With radium as application, the most suitable DFT methods have been selected by comparison with structures and interaction energies determined by state-of-the-art calculations. Scarce Ra^{2+} complexation constants are available, but combined through isodesmic-like reactions (*e.g.* transmetallation), they allow for error cancellation mechanisms. Then, a radiometal-specific cavity is fitted in an implicit solvent model to reproduce solvation effects. The equilibrium constants can finally be calculated accurately, *i.e.* with a precision of 1 logarithmic unit, provided that the relativistic spin–orbit interaction is taken into account. The relevance of this methodology is illustrated with macropa, an 18-membered macrocyclic ligand recently considered for developing ^{223}Ra radiotherapeutics, highlighting that the design of an innovative chelator by assuming transferability of neighboring element chemistry can only be suboptimal.

Introduction

Radioelements are special elements, they have only radioactive isotopes. Those with short-lived isotopes ($<$ several years) are of particular interest to chemists. On the one hand, they can be used for applications based on their radiation alone or for the combination of chemical properties and their radiation. On the other hand, they can be toxic to humans, which requires a better understanding of their behavior. The behavior of radio-nuclides in the environment or in living organisms is linked, at the molecular level, to their speciation, *i.e.* their specific chemical form(s). However, the quantities handled do not allow the use of classical techniques to evaluate the chemical forms of the elements. In this context, molecular modelling is a particularly interesting tool to use, prior to, in parallel with or after the experiments. A recent tour de force was the identification, assisted by quantum mechanical calculations, of the

very first halogen bonds involving astatine.[1,2] The Pourbaix diagram (potential-pH) of this radioelement could also not have been established without coupling modelling to experiments.[3,4] Among other recent examples, it is the comparison of the spectral signatures with those from theoretical calculations which allowed to conclude on the nature of the predominant forms of polonium(IV) in concentrated hydrochloric acid solution.[5] *In silico* simulations can also provide thermodynamic data such as diffusion coefficients, solvation energies, as recently demonstrated in the series of tetravalent actinides, from thorium(IV) to berkelium(IV).[6]

A particularly interesting radioelement that has been studied very little is radium.[7] Discovered by Marie and Pierre Curie in 1898, it has natural isotopes ^{223}Ra, ^{224}Ra, ^{226}Ra and ^{228}Ra that come from primordial uranium and thorium decay chains.[8] ^{226}Ra is one of the most widespread alpha-emitters in environment, as well as one of the most toxic.[9] Radium is highly mobile in the environment considering its high solubility and its poor reactivity similar to other alkaline-earth metals. Belonging to the alkaline-earth family, it follows the behaviour of calcium after ingestion in human body, which might lead to an important internal radiation dose. Given its toxicity, the need to understand the behaviour of radium in the environment is of particular interest, notably in relation to the management of TE-NORM (Technologically

[a] *Nantes Université, CNRS, CEISAM UMR 6230, F-44000 Nantes, France.*
  E-mail: nicolas.galland@univ-nantes.fr
[b] *IMT Atlantique, CNRS, SUBATECH UMR 6457, F-44307 Nantes, France*
[c] *TRISKEM INTERNATIONAL, F-35170 Bruz, France*
† Electronic supplementary information (ESI) available: Computed structures, and supporting figures and tables. See DOI: https://doi.org/10.1039/d3nj02103c

Enhanced Naturally Occurring Radioactive Material) products, which mainly originate from uranium mining/milling and other industrial exploitation of phosphate, fossil fuels, *etc.*[10] In this context, one of the current challenges is to set up methods for rapid and quantitative analysis of environmental radium. As recently outlined,[11] there is an urgent need to develop supports capable of trapping Ra directly in natural waters, which requires in particular a selectivity towards other alkaline-earth and rare-earth metals. This involves the building of specific chelating agents following a molecular recognition technology approach, which itself requires a thorough knowledge of the coordination properties of Ra.

The development of such chelates is also an issue in nuclear medicine. Indeed, the [223]Ra radionuclide is the first and currently only approved alpha-emitting drug for therapy.[12] Administered as a chloride salt, $[^{223}Ra]Ra^{2+}$ is readily incorporated into bone turnover sites, including sites of osseous metastatic castrate-resistant prostate cancer, where its decay irradiates the malignant tissues. The established clinical efficacy, safety, and availability of [223]Ra motivate efforts towards applying more broadly this radionuclide, *i.e.* in a capacity that is independent of its biodistribution properties by means of coupling to a biological targeting vector.[13] This requires the development of a bifunctional chelator (BFC), which forms a stable linkage between the radionuclide and the vector molecule. The BFC presents a complex extracting the radionuclide from its solution and guarantees its stable immobilization *in vivo*. A great interest exists in the field of inorganic chemistry for developing target specific radiopharmaceuticals, knowing that a fundamental critical component is each metal ion has its own specific coordination chemistry requirements (coordination number, geometry, donor atom preferences and ionic/covalent bond contribution).[14,15]

As a result, the need to better understand the coordination chemistry of Ra is of great interest for environmental and medical issues. Indeed, the chemistry of radium in solution is typically inferred from that of its closest alkaline-earth metal, barium, which presents stable isotopes.[16,17] Molecular modelling can be a tool of choice to assist and guide the rational design of radiometal-specific chelators and,[18–22] in the case of Ra^{2+}, is certainly less expensive and more flexible than experiments realized on its non-radioactive surrogate, Ba^{2+}. This work goes beyond the few previous theoretical investigations of the chemistry of Ra.[23–27] It presents an approach for tailoring a relativistic-quantum-mechanical-based low-cost methodology that allows for the accurate study of its coordination chemistry, which is generalizable to any other metallic radioelements.

Computational details

The most accurate approach to incorporate relativity would be to perform four-component quantum mechanical calculations based on the exact one-electron relativistic Hamiltonian. Nevertheless, several alternative two-component (2c) approximations have been developed and used to efficiently treat relativistic effects.[28] There is also a long-standing interest in using density

functional theory (DFT) methods when considering systems of several dozen atoms. In 2c-DFT approaches based on Kohn–Sham equations, the orbital representation is replaced by spinors $\varphi_i(r)$ that are vector functions of two components:

$$\varphi_i(r) = \begin{pmatrix} \varphi_i^\alpha(r) \\ \varphi_i^\beta(r) \end{pmatrix} = \begin{pmatrix} \sum_\mu c_{i\mu}^\alpha \chi_\mu(r) \\ \sum_\mu c_{i\mu}^\beta \chi_\mu(r) \end{pmatrix}$$

The latter are usually expanded using atom-centered Gaussian basis functions χ_μ, and the expansion coefficients c_i are complex and determined within the variational procedure. Relativistic effects are usually split in two categories, spin-independent (scalar) effects and spin-dependent effects. The scalar-relativistic effects are essentially associated with the relativistic mass increase of the electrons, resulting from their high speed near the nucleus. The main spin-dependent effect is the so-called spin–orbit coupling (SOC). 2c-DFT methods can take advantage of relativistic effective core potentials (RECPs), which replace inner-core electrons and introduce scalar and, optionally, spin–orbit terms into the variational procedure. There can be many variations in the form of RECPs, the present ones are expressed as follows:[29]

$$\hat{V}(r) = -\frac{Z_{\text{eff}}}{r} + \sum_{klj} B_{lj}^k \exp\left(-\beta_{lj}^k r^2\right)\hat{P}_{lj}$$

where Z_{eff} is the charge of the inner-core. The sum runs over a Gaussian expansion (index k) of semi-local short-range radial potentials, which are different for different orbital angular-momentum quantum numbers l, and, for a given l, for the two total one-electron angular-momentum quantum numbers $j = l \pm \frac{1}{2}$. $\hat{P}_{lj}$ is the 2c projector onto the entire space of functions with angular symmetry l, j around the core under study. The parameters B_{lj}^k and β_{lj}^k are adjusted to reproduce results of atomic all-electron four-component calculations. The Generalized Kohn–Sham (GKS) method, implemented in the Gaussian 16 program,[30] makes use of such RECPs, while the omission of their spin–orbit terms leads to scalar-relativistic (sr) only calculations.

If DFT is particularly attractive because of its computational expediency, one has to deal with the shortcomings of the density functional approximations used for the exchange–correlation term in the Kohn–Sham equations. It is important to know which functionals can be safely used to study radium compounds. Fifteen recent and popular DFT functionals based on generalized gradient approximations (GGAs) have been tested: five global hybrid GGAs (GH GGAs: B3LYP,[31] B3PW91,[32] mPW3PBE,[33] PBE0,[34] B98[35]), seven global hybrid meta-GGAs (GH meta-GGAs: TPSSh,[36] τ-HCTHh,[37] BMK,[38] PW6B95,[39] M06-2X,[40] M08-HX,[41] MN15[42]), and three range-separated hybrid GGAs (RSH GGAs: HSE03,[43] HSE06,[44] ωB97X[45]). Two sets of basis function have mainly been used. The ACVDZ set of valence double zeta quality combines the aug-cc-pCVDZ-PP basis sets for the Ra and Ba atoms,[29,46] the aug-cc-pVDZ basis sets for the O and N atoms, and the cc-pVDZ basis sets for the remaining atoms.[47–49] The ACVTZ set of valence triple zeta quality combines the aug-cc-pCVTZ-PP basis sets for the Ra and Ba atoms,[29,46] the aug-cc-pVTZ basis sets for the O and N atoms, and the cc-pVTZ basis sets for

the remaining atoms.[47–49] Note that for comparison purposes, additional *ab initio* calculations have been performed using the ACVQZ and ACV5Z sets of basis function, which are the valence quadruple and quintuple zeta variants of the previous sets. The CCSD(T) method is extremely reliable in most instances, and it has come to be the effective "gold standard" for single reference calculations.[50] The CCSD(T) computations used the frozen-core approximation, *e.g.*, the 6s6p electrons of Ra were kept uncorrelated as well as the 1s electrons of O atoms. For studied species, an estimate of the CCSD(T) energy at the complete basis set limit (CBS) was produced by combining:

• The Hartree–Fock energy obtained from the three-point extrapolation formulae of Feller:[51]

$$E_X = E_{CBS} + Be^{-\alpha X}$$

where X is the cardinal number of the basis sets, *e.g.*, 3 for ACVTZ, 4 for ACVQZ and 5 for ACV5Z. The E_{CBS} energy, α and B parameters are then determined from three computed Hartree-Fock energies.

• The correlation energy obtained from the two-point extrapolation scheme USTE $(x - 1, x)$ of Varandas and co-workers:[52]

$$E_X^{corr} = E_{CBS}^{corr} + \frac{A}{x^3}$$

where x is simply referred as hierarchical number. In case of coupled cluster calculations, $x = 3.68$ when $X = 4$ and $x = 4.71$ when $X = 5$. The two correlation energies from CCSD(T) calculations using ACVQZ and ACV5Z basis sets, allowed us to determine both the A parameter and the E_{CBS}^{corr} correlation energy.

The influence of the solvent was taken into account using an implicit solvation model, namely the solvation model based on solute density (SMD).[53] SMD is said universal since it is applicable to any charged or uncharged solute in any solvent, but as well as other current continuum models, it does not have radium-specific parameters for the construction of the solute cavity. The solute cavity is an important part of the model, this issue will be addressed later. For each species, its Gibbs free energy in solution is obtained by adding the gas phase free energy and the solvation free energy. For computing the latter, the solute's geometry was optimized separately in vacuum and within the SMD model, at the scalar-relativistic level of theory. Note that in case of species characterized by several competitive conformers, their free energies have been evaluated using a Boltzmann distribution:

$$G_{\{S\}} = -RT \ln \left(\sum_{i \in \{S\}} \exp(-G_i/RT) \right)$$

where the summation runs over all the conformers of each S species.

Results and discussion

This work proposes a strategy to establish a computational methodology that is both cost effective and tailored for a given metallic radioelement, the coordination of which is under study. This strategy is illustrated here on the case of radium, both as a radioelement and a heavy metal. The selection of the quantum mechanical calculation methods is first performed. It is guided by comparisons with reference data, either from experiments or from state-of-the-art calculations performed on relevant Ra(II) complexes. Then the question of the solvent model is addressed. Implicit models can accurately reproduce the influence of the environment at reduced computational time, provided that adjustments specific to the studied radiometals are anticipated. The relevance of the introduced parameters will be verified by comparison between calculated and measured equilibrium constants for reactions involving a wide range of ligands (neutral, anionic, macrocyclic or not, functionalized with oxygen and/or nitrogen atoms, of environmental or nuclear medicine concern). The targeted precision on the value of the constants in solution is 1 in log unit (error less than 6 kJ mol^{-1} on the Gibbs free energy scale at 298 K). Finally, the contribution of relativistic effects will be discussed.

To conclude, the usefulness and importance of the established methodology will be illustrated with the study of a macrocyclic considered for the vectorization of ^{223}Ra in nuclear medicine.[13]

Geometric benchmark

In this section, 15 popular or recent DFT functionals are evaluated on their ability to accurately describe the interaction geometries involving Ra^{2+} or its closest analogue, Ba^{2+}, which is usually considered as an experimental surrogate to understand the chemistry of radium.[17] It is therefore necessary that the computational methodology takes this into account, *i.e.* that it is also adapted to describe accurately the coordination properties of Ba(II) in solution. Reference structures have been defined according to some constraints and choices. Chart 1 shows the crystallographic structures of Ba^{2+} complexed with a macrocycle that were extracted from the Cambridge Structural Database (CSD).[54] These two structures show interactions with carboxylic functions and nitrate ions, representative of the compounds present in environmental samples or introduced by current extraction technologies used for Ra decontamination. The selected interaction distances from these two structures are displayed in ESI,† in Fig. S1. Unlike to Ba^{2+}, no crystallographic structure exists for Ra^{2+} complexed with macrocycles. Hence, reference structures made of Ra(II) were obtained through scalar-relativistic quantum calculations using the gold standard CCSD(T) method (see ESI†). The selected ligands are the water molecule and the carbonate
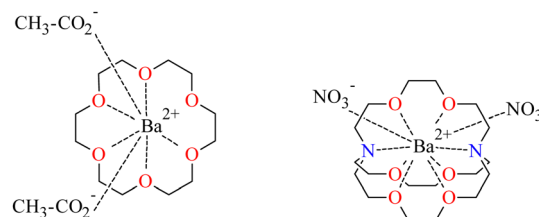

Chart 1 Structures of CSD entries BIWBAK (left) and AZELOG (right).

Table 1 Computed reference structures at the sr-CCSD(T)/ACVTZ level of theory: symmetry and interaction distances

	Ra–O distance (Å)	Symmetry
$RaCO_3$	2.376	C_{2v}
$RaSO_4$	2.584	C_{3v}
$[RaH_2O]^{2+}$	2.690	C_{2v}

(CO_3^{2-}) and sulphate (SO_4^{2-}) anions, given their important role in natural environment (both surface and groundwater) and the particular affinity of radium for the oxygen heteroatom. The interaction distances between radium and oxygen atoms are presented in Table 1. It should be noted that the radium coordination is 2 in the $RaCO_3$ structure, corresponding to a C_{2v} symmetry, and 3 in the $RaSO_4$ structure, corresponding to a C_{3v} symmetry.

The structures of the reference complexes have been optimized at the scalar-relativistic level using the ACVDZ set of basis function and 15 DFT functionals. For assessing the accuracy of each functional, the computed interaction distances between the metal, Ra or Ba, and its neighboring heteroatoms, O and N, are compared to the CCSD(T) distances and the crystallographic distances (CSD entries BIWBAK and AZELOG). For each distance, the absolute error is converted in percentage (APE, see Table S1 in ESI†), and mean values (MAPEs) are calculated in Table 2 for all interaction distances with Ra, for all interaction distances with Ba, or considering all interaction distances. The average MAPE value (Table 2, last column) range between 1.3% and 2.3%, showing that all DFT functionals accurately describe the geometric parameters of the metal-ligand interaction. Considering especially the Ra(II) complexes, the difference between the smallest and the largest MAPE values is also about 1%. The case is similar for Ba(II) complexes, but the MAPE values are 1.1% higher on average. One may think that Ra(II) complexes are better described, but the comparison of Ba(II) crystallographic structures with DFT ones that do not consider the crystal environment is somewhat biased. Overall, the performances of the selected functionals do not differ significantly from each other and the reference structures are well reproduced, which does not allow us to discriminate between the 15 DFT functionals.

Table 2 MAPE values for computed M–X interaction distances (M = Ra, Ba and X = O, N) using several DFT functionals and the ACVDZ set of basis functions

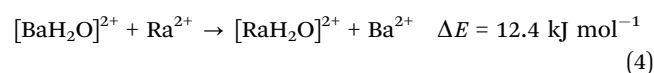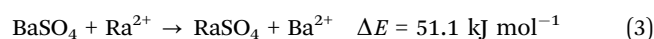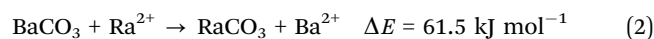| DFT functional	Ra–O	Ba–X	Average
MN15	0.6	1.9	1.3
HSE03	0.7	1.8	1.3
PBE0	0.7	1.9	1.3
HSE06	0.7	1.9	1.3
PW6B95	0.9	1.9	1.4
mPW3PBE	0.9	2.0	1.4
B3PW91	1.0	2.1	1.5
TPSSh	1.1	2.0	1.5
BMK	1.0	2.0	1.5
M08-HX	1.3	1.8	1.5
τ-HCTHhyb	1.1	2.3	1.7
B98	1.3	2.3	1.8
M06-2X	0.8	2.8	1.8
B3LYP	1.7	2.2	1.9
ωB97X	1.3	3.3	2.3

However, it is found that the ωB97X and M06-2X functionals lead to a change of Ba coordination when optimizing the AZELOG geometry (from 10 to 12). It partly explains the larger MAPE values for these functionals. Some improvement can be expected if they are used in conjunction with more complete basis sets. It was quantified for the functionals with the largest MAPEs, B3LYP and ωB97X, by reoptimizing the geometries of the Ra(II) complexes with the ACVTZ set of basis function. The results obtained with the ACVDZ and ACVTZ sets can be compared from the Table S2 (see ESI†), showing a clear improvement: MAPE is at most 0.4% for B3LYP and ωB97X. These functionals, as well as M08-HX, may require triple-zeta valence quality basis functions for optimal description of interaction geometries. Regarding MN15, PBE0 and PW6B95, previously among the best performing DFT functionals, the comparison between ACVDZ and ACVTZ results (Table S2, ESI†) does not show systematic improvements. The MAPE slightly increases for MN15 (+0.1%) and it is unchanged for PBE0. Overall, the ACVTZ basis set does not lead to significant improvements of the interaction distances, at the cost of a much higher computation time. The ACVDZ calculations already yield accurate structures.

Benchmark on interaction energies

The benchmark on interaction geometries is not discriminating regarding the 15 studied DFT functionals, but they were also evaluated on their ability to accurately describe interaction energies. The latter correspond to reactions of complexation between Ra^{2+} or Ba^{2+} and previous model ligands (SO_4^{2-}, CO_3^{2-} and H_2O). Note that these DFT functionals are not expected to predict the exact interaction energies with high accuracy. Instead, we focus on their ability to describe the relative evolution of interaction energies in a series of complexes. In order to benefit from a partial cancellation of systematic errors in the calculations of the electron correlation and relativistic contributions to the metal–ligand interactions, isodesmic-like reactions have been considered. At first, we studied an exchange reaction of equally charged ligands:

$$RaSO_4 + CO_3^{2-} \rightarrow RaCO_3 + SO_4^{2-} \quad \Delta E = -116.9 \text{ kJ mol}^{-1} \tag{1}$$
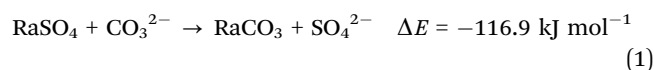
This category of reaction is particularly relevant when one wishes to compare the affinity of a metal with respect to different ligands or chelators. We also considered a second category of reactions close to transmetallation, where metals are exchanged for quantifying the selectivity of a ligand or a chelator. Here, we focused on the competition between Ra^{2+} and its non-radioactive surrogate, Ba^{2+}:

$$BaCO_3 + Ra^{2+} \rightarrow RaCO_3 + Ba^{2+} \quad \Delta E = 61.5 \text{ kJ mol}^{-1} \tag{2}$$

$$BaSO_4 + Ra^{2+} \rightarrow RaSO_4 + Ba^{2+} \quad \Delta E = 51.1 \text{ kJ mol}^{-1} \tag{3}$$

$$[BaH_2O]^{2+} + Ra^{2+} \rightarrow [RaH_2O]^{2+} + Ba^{2+} \quad \Delta E = 12.4 \text{ kJ mol}^{-1} \tag{4}$$

The presented reference energies for reactions (1)–(4) have been determined at the sr-CCSD(T)/CBS level of theory (see

Table S3 in ESI†), based on geometries previously optimized at the sr-CCSD(T)/ACVTZ level of theory. Then, reaction energies for each DFT functional and the two sets of basis function (ACVDZ and ACVTZ) have been obtained using the previous sr-DFT/ACVDZ geometries. For each reaction, the absolute error on the reaction energy is expressed in percentage (APE, see Table S4 in ESI†), and the mean value (MAPE) is presented in Table 3 for each functional. MAPEs are larger and more spread than those in geometric benchmark. For instance, the MAPE values range between 4.6% (BMK) and 18.2% (B3LYP) when using the ACVDZ basis set. The interaction energies appear therefore as a more discriminating criterion when it comes to the choice of the DFT functional. With the ACVDZ basis set, the MAPE values are therefore always bigger than 4%. A significant improvement is observed with single-point calculations using the ACVTZ basis set: MAPEs values are reduced on average by 3.5%. Moreover, four of the 15 studied functionals yield now MAPEs below 4%: ωB97X, M08-HX, MN15 and PW6B95. Hence, the latter appear the most accurate for describing interaction energies.

If the ωB97X functional seems particularly accurate (smallest MAPE, 1.4%), it cannot be said for the two other RSH GGA functionals, HSE06 and HSE03 (MAPEs respectively of 7.6% and 8.3%). It can be seen that the first one relies at 100% on the "exact" exchange in the long-range limit, while the amount of exact exchange drops to 0 in the long-range component of the screened exchange HSE functionals. Furthermore, the next five best functionals are GH meta-GGAs showing in general high fractions of exact exchange (e.g., 52.23% for M08-HX, 44% for MN15). However, the fourth ranked functional PW6B95 (MAPE of 3.9%) has an exact exchange fraction of only 28%. All studied GH GGAs yield relatively high MAPE values, the PBE0 functional being the best ranked in this category (MAPE of 7.5%).

Note that the GH meta-GGAs M06-2X and BMK, having an exact exchange fraction greater than 42%, perform rather well with the ACVDZ basis set (MAPEs of 5.4% and 4.6%, respectively). They would be an attractive alternative to ωB97X, M08-HX, MN15 and PW6B95 for the study of interactions with large chelators, where the use of double-zeta basis sets is unavoidable.

Table 3 MAPE values for calculated interaction energies using several DFT functionals and sets of basis functions

DFT functional	Basis set	
	ACVDZ	ACVTZ
ωB97X	7.0	1.4
M08-HX	4.9	2.7
MN15	8.6	3.5
PW6B95	9.2	3.9
M06-2X	5.4	6.8
TPSSh	12.4	7.2
PBE0	11.7	7.5
HSE06	11.8	7.6
B98	12.4	8.1
HSE03	12.4	8.3
τ-HCTHhyb	13.3	8.3
B3PW91	13.2	8.5
mPW3PBE	13.3	8.7
B3LYP	18.2	10.1
BMK	4.6	13.9

Assessment of the solvent model

The ωB97X, M08-HX, MN15 and PW6B95 functionals represent the best compromise, if interaction energies are computed using the ACVTZ basis set on geometries optimized with the ACVDZ basis set. The next step towards the completion of the computational methodology is to tackle the solvent effects. The most cost-effective approach to simulate the influence of a solvent is probably to use continuum models. Within this category, the SMD model was built to accurately predict solvation energies for uncharged and ionic solutes in a wide range of solvents.[53] However, this advantage is conditioned by the existence of parameters for the solute specifically adapted to the representation of the solute–solvent boundary. In the SMD solvation model, each element has a defined Coulomb radius, i.e. a radius defining a sphere which, combined with analogous spheres of the other elements constituting the solute, forms the solute cavity in the solvent. But for heavy elements such as radium, no Coulomb radii have been derived when SMD was originally parametrized. Note that the situation is similar for other continuum models popular in the quantum chemistry. Thus, the ability of these models to simulate the influence of solvents on Ra(II) compounds is questioned.

Let us first consider barium since more trusted experimental data are available compared to radium. For instance, several consistent values of aqueous solvation Gibbs free energy were reported for Ba^{2+}: -1354.9 kJ mol^{-1},[55] -1359.6 kJ mol^{-1},[56] and -1359.6 kJ mol^{-1}.[57] Note that these values are adjusted according to the conventions used in the SMD model, i.e. (i) 298.15 K temperature and the standard state of an ideal gas at a gas-phase concentration of 1 mol L^{-1} dissolving as an ideal dilute solution at a liquid-phase concentration of 1 mol L^{-1}, and (ii) absolute solvation energies rely on the Tissandier et al. solvation free energy of the proton.[58] The SMD model has then been tested on its ability to calculate the aqueous solvation energy of Ba^{2+}, according to the recommendation that any ion containing three or fewer atoms must be clustered with a single water molecule (see ref. 53). The solvation free energy for Ba^{2+} is then determined as:

$$\Delta G^*_{sol}(Ba^{2+}) = \Delta G^*_{sol}\left([Ba(H_2O)]^{2+}\right) + \Delta G^{\circ}_{g}(B.E.) - \Delta G^*_{sol}(H_2O) - \Delta G^{\circ \to *} - RT \ln 55.34$$

The three last terms do not require any quantum chemical calculations:[59] $\Delta G^*_{sol}(H_2O)$ is the aqueous solvation free energy of water (-26.5 kJ mol^{-1}), $\Delta G^{\circ \to *}$ is the free energy change associated with moving from a gas-phase pressure of 1 atm to a liquid-phase concentration of 1 mol L^{-1} (7.9 kJ mol^{-1}), and the water concentration (55.34 mol L^{-1}) is taken into account in the final corrective term. Conversely, sr-DFT/ACVDZ calculations have been performed to determine $\Delta G^*_{sol}\left([Ba(H_2O)]^{2+}\right)$ and $\Delta G^{\circ}_{g}(B.E.)$, i.e. the solvation free energy of the clustered Ba^{2+} ion and its gas-phase binding free energy, respectively. Geometries were optimized in vacuo, followed by an optimization within the SMD model for calculating $\Delta G^*_{sol}\left([Ba(H_2O)]^{2+}\right)$, or followed by 2c-DFT/ACVTZ energy calculations for improving the $\Delta G^{\circ}_{g}(B.E.)$ value. The resulting solvation

free energies of Ba^{2+} obtained with the four best performing functionals are presented in Table 4.

With the default Coulomb radii of barium, the $\Delta G_{sol}^*(Ba^{2+})$ values range from -1500 to -1505 kJ mol^{-1}. The deviation from the mean experimental value, -1358 kJ mol^{-1}, is bigger than 140 kJ mol^{-1}, which is not satisfactory at all. We propose to adjust a Coulomb radius within the SMD model that is specific to barium. The results obtained with four alternative radii are presented in Table 4. The value of r_{Ba} = 2.045 Å best reproduces the experimental $\Delta G_{sol}^*(Ba^{2+})$ values for the 4 DFT functionals, since it yields a mean Gibbs energy of solvation of -1358.8 kJ mol^{-1}. The standard deviation between calculated values, 2.5 kJ mol^{-1}, is similar to that between experimental values, 2.7 kJ mol^{-1}. However, the usefulness of this Coulomb radius for Ba needs to be verified. The retained criterion is the comparison between experimental and calculated equilibrium constants in aqueous solution.

Previously, the interest of studying exchange reactions of equally charged ligands has been discussed from a computational point of view:

$$[BaL_1]^{2-x} + L_2^{x-} \rightarrow [BaL_2]^{2-x} + L_1^{x-} \qquad (5)$$
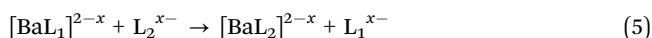
The sulfate anion is considered again as L_1, and the complexation of Ba^{2+} with the oxalate ligand (as L_2) was studied experimentally under the same conditions.[60] It is therefore possible from the respective formation constants to have an accurate experimental estimate of the equilibrium constant K_{exc} for reaction (5). Regarding molecular modeling, K_{exc} is calculated from the free energy of reaction in solution, ΔG_s^*, which in turn is obtained from a thermodynamic cycle involving this same gas-phase reaction and solvation steps of the species involved. sr-DFT/ACVDZ calculations have been performed to determine the gas-phase vibrational frequencies and geometries of each species, and 2c-DFT/ACVTZ energy were calculated for these geometries, in order to compute the gas-phase free energy of reaction, ΔG_s°. The solvation free energies ΔG_{sol}^* have been obtained through sr-DFT/ACVDZ geometry optimizations within the SMD model. However, according to the seminal SMD paper,[53] ligands such as SO_4^{2-} and $C_2O_4^{2-}$ (one or more oxygen atoms bearing a partial atomic charge more negative than the charge on oxygen in water) must be clustered with one or more water molecules. ΔG_s^* is thus determined using the thermodynamic cycle shown in Scheme 1, where n and m represent the numbers of water molecules used for the hydration of Ba(II) complexes and free ligands, respectively. As explained elsewhere,[59] the $\Delta G^*(i)$ (i = a, b, c, d) terms
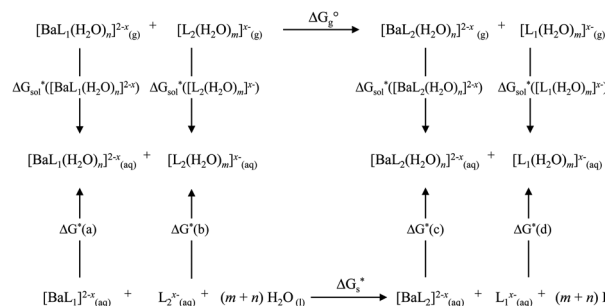
Scheme 1 Hess cycle used to calculate the Gibbs energy of the reaction (5) with explicitly treated solvent molecules.

corresponding to the formation of solvated clusters in liquid water are null. It then comes:

$$\Delta G_s^* = \Delta G_g^\circ + \Delta G_{sol}^*\left([BaL_2(H_2O)_n]^{2-x}\right) + \Delta G_{sol}^*\left([L_1(H_2O)_m]^{x-}\right) \\ - \Delta G_{sol}^*\left([BaL_1(H_2O)_n]^{2-x}\right) - \Delta G_{sol}^*\left([L_2(H_2O)_m]^{x-}\right)$$

By proceeding in this manner, the estimate of ΔG_s^* benefits from partial cancellations of systematic errors in the computations on the species on the left and right sides of the reaction (5). For instance, (i) the errors on the entropic contribution to the Gibbs energy differ depending on whether a ligand or its complex is studied (presence of soft vibrational modes), and (ii) the SMD model is systematically more accurate for neutral solutes than for charged ones.[53] In addition, the more similar the L_1 and L_2 ligands are, the better the errors are compensated.

As a first approach, the anions were clustered with one water molecule (m = 1). However, the water molecule interacts somewhat differently between the oxygen atoms of sulfate and those of oxalate (see Fig. S2 in ESI†), leading to an unbalanced exchange reaction. The difference can be partially compensated by clustering each Ba(II) complex also with one water molecule (n = 1). Table 5 presents the equilibrium constant K_{exc} determined with three of the DFT functionals, together with the experimental value. The deviation between calculated values of $\log K_{exc}$ and the experimental value is satisfactory: the smallest deviation is 0.34 with the ωB97X functional, and the mean deviation is 0.68. Note that improving the description of specific solute–solvent interactions, for example by explicitly treating a second water molecule from the first solvation layer, should improve the agreement with experiment. For instance, the deviation decreases with the MN15 functional from 0.75 to 0.45 when m = 2 and n = 2. This first results validate the choice of the adjusted value of r_{Ba}.

A second attempt of validation is proposed by looking at the data in Table 5, $i.e.$ the comparison between calculated and experimental constants of an exchange reaction between neutral nitrogen ligands. The equilibrium constants for the complexation of Ba^{2+} with 1,10-phenanthroline and 2,2'-bipyridine have been measured under the same conditions (298 K, ionic strength of 0.25 M),[61] providing an accurate estimate of the exchange reaction constant: $\log K_{exc}$ = -0.81 ± 0.10. The mean value obtained from the DFT calculations is -1.03, that is a deviation

Table 4 Calculated Gibbs free energies (in kJ mol^{-1}) of aqueous solvation for Ba^{2+} using the SMD implicit model with selected DFT functionals

| DFT functional | Ba Coulomb radius | | | | |
	2.030 Å	2.040 Å	2.045 Å	2.050 Å	Default value
ωB97X	-1368.4	-1362.2	-1359.1	-1356.0	-1501.1
M08-HX	-1367.4	-1361.2	-1358.1	-1355.1	-1501.2
MN15	-1371.5	-1365.2	-1362.1	-1359.1	-1505.0
PW6B95	-1365.3	-1359.0	-1356.0	-1352.9	-1499.7
Average	-1368.1	-1361.9	-1358.8	-1355.8	-1501.7

Table 5 Calculated values of log K_{exc} for the exchange reaction (5), using the SMD implicit model (r_{Ba} = 2.045 Å) and selected DFT functionals

	$L_1 = SO_4^{2-}$, $L_2 = C_2O_4^{2-}$	L_1 = 1,10-phenanthroline, L_2 = 2,2′-bipyridine
exp.	−0.08[60]	−0.81 ± 0.10[61]
ωB97X	0.26	−1.08
M08-HX	0.88	−0.98
MN15	0.67	−1.04

of only 0.22. Although the SMD model does not require adding solvent molecules to the species involved in this exchange reaction (no ion made of few atoms and no oxygen atoms bearing a significant atomic charge), considering the specific interaction between the charged Ba(ɪɪ) complexes and one water molecule (m = 0 and n = 1) can improve the agreement with experiment. The computed structures with the MN15 functional for the most stable conformations are shown in Fig. 1. The log K_{exc} value then changes from −1.04 to −0.93. Thus, the relevance of the SMD model to help predict equilibrium constants is confirmed for heavy metals, provided that specific Coulomb radii are available.

Determining a cavity for radium

The accurate description of the coordination chemistry of Ra(ɪɪ) in solution therefore requires the determination of an optimal r_{Ra} Coulomb radius, consistently to the SMD model. However, it cannot be done in the same way as with the barium since no consensus exists on the free energy of aqueous solvation of Ra^{2+}. Some authors propose a value for $\Delta G_{sol}^*(Ra^{2+})$ nearly equal to that of $\Delta G_{sol}^*(Ba^{2+})$,[55,57] while a significantly weaker value for $\Delta G_{sol}^*(Ra^{2+})$, by 34.7 kJ mol^{-1}, is expected from the data of R. M. Noyes.[62] As an alternative, the value of r_{Ra} can be fitted on the basis of a homogeneous set of experimental complexation constants. Matyskin *et al.* have recently investigated the interactions with hydroxide and ethylenediaminetetraacetic acid (EDTA), providing complexation constants at zero ionic strength and 25 °C.[63,64] The experiments having been done with both Ra^{2+} and Ba^{2+}, we can return to the study of exchange reactions between the two metals in order to benefit from mechanisms of error cancelation in the calculations, as discussed previously. The thermodynamic cycle used to compute the Gibbs free energy of each exchange reaction in aqueous solution is shown in Scheme 2, where L = HO$^-$ or EDTA^{4-}.
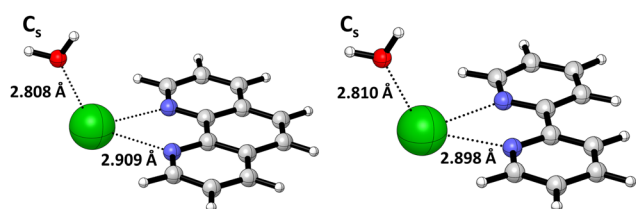

Fig. 1 Computed structure at the SMD sr-MN15/ACVDZ level of theory for the most stable conformation of a water molecule added to the Ba(ɪɪ) complex with 1,10-phenantroline (left) and with 2,2′-bipyridine (right).

It comes:

$$\Delta G_s^* = \Delta G_g^\circ + \Delta G_{sol}^*\left([BaL(H_2O)_n]^{2-x}\right) \\ + \Delta G_{sol}^*\left([Ra(H_2O)_m]^{2+}\right) - \Delta G_{sol}^*\left([RaL(H_2O)_n]^{2-x}\right) \\ - \Delta G_{sol}^*\left([Ba(H_2O)_m]^{2+}\right)$$

sr-DFT/ACVDZ calculations have been performed to determine the gas-phase vibrational frequencies and geometries of each species, and 2c-DFT/ACVTZ energy were calculated for these geometries, in order to compute the gas-phase free energy of reaction, ΔG_g°. The solvation free energies ΔG_{sol}^* have been obtained through sr-DFT/ACVDZ geometry optimizations, using in the SMD model r_{Ba} = 2.045 Å for Ba species and four different values of r_{Ra} for Ra species. Following the guidelines for use of the SMD model, all species have been clustered with one water molecule for the reaction with L = HO$^-$, *i.e.* m = 1 and n = 1. The computed structures with the MN15 functional for the most stable metal complexes are shown in Fig. 2. All species have also been clustered with one water molecule in case of L = EDTA^{4-} (m = 1 and n = 1). In the experimental conditions, note that Na$^+$ cations were part of the ionic medium, their concentration was considerably higher than that of Ra^{2+} and Ba^{2+}, and the effect of complex formation between EDTA^{4-} and Na$^+$ is important.[63] This led to also considering a Na$^+$ cation in the environment of the complexes formed by EDTA^{4-} (see Fig. S4 in ESI†). For the four best-performing DFT functionals, Table 6 presents the equilibrium constants determined with each r_{Ra} value, while Table S5 (see ESI†) presents the calculated absolute errors with respect to the experimental values.

Considering all the results, *i.e.* without differentiating the DFT functionals and the r_{Ra} values, the errors are significantly smaller for the reaction with L = HO$^-$. The mean absolute error on log K_{exc} is MAE$_1$ = 0.22, while for the exchange reaction with L = EDTA^{4-}, MAE$_2$ = 0.39. The objective is to identify a r_{Ra} value that leads to the best agreement with the two experimental constants, whatever the DFT method. As a criterion, we have defined for a given Coulomb radius a weighted mean of absolute error:

$$WMAE(r_{Ra}) = \frac{1}{4}\sum\left(\frac{MAE_2}{MAE_1 + MAE_2}AE_1(r_{Ra})\right. \\ \left. + \frac{MAE_1}{MAE_1 + MAE_2}AE_2(r_{Ra})\right)$$
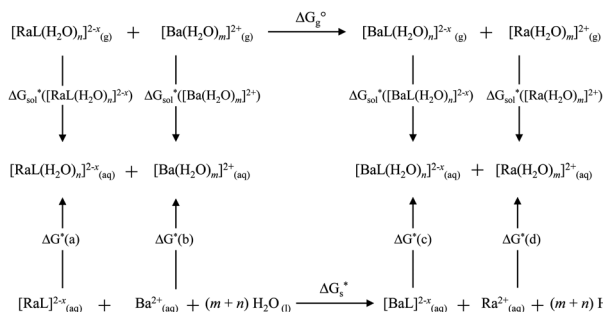
Scheme 2 Hess cycle used to calculate the Gibbs energy of the exchange reactions between Ra^{2+} and Ba^{2+} with explicitly treated solvent molecules.
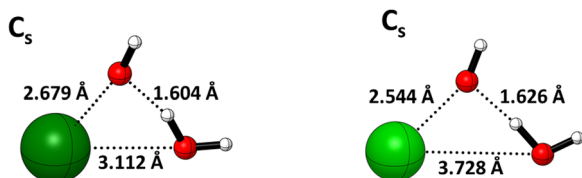
Fig. 2 Computed structure at the SMD sr-MN15/ACVDZ level of theory for the most stable conformation of $[RaOH(H_2O)_1]^+$ (left) and $[BaOH(H_2O)_1]^+$ (right).

where the summation runs over the 4 DFT functionals, and for a given functional, $AE_1(r_{Ra})$ and $AE_2(r_{Ra})$ are the absolute errors corresponding to the reactions with $L = HO^-$ and $L = EDTA^{4-}$, respectively. The WMAE values are reported in Table 6 for each Coulomb radius tested within the SMD solvent model. The lowest WMAE is obtained for $r_{Ra} = 2.110$ Å, with a value of 0.23 corresponding to 1.3 kJ mol^{-1} on the Gibbs free energy scale at 298 K.

The relevance of the adjusted Coulomb radius for Ra can be verified through further comparisons to experimental data. For instance, the previous study of exchange reactions between Ra^{2+} and Ba^{2+} led us to calculate the difference of solvation free energies between Ra^{2+} and Ba^{2+}. According to the ωB97X, M08-HX, MN15 and PW6B95 computations, $\Delta G^*_{sol}(Ra^{2+})$ is on average 39.2 kJ mol^{-1} weaker than $\Delta G^*_{sol}(Ba^{2+})$. This result is in line with the trend of decreasing solvation free energy in the series of alkaline-earth metals, and it is also in good agreement with the value of 34.7 kJ mol^{-1} obtained from the data of R. M. Noyes.[62]

In addition, the reliability of $r_{Ra} = 2.110$ Å is further assessed against results obtained with aqueous crown ethers. The possible use of crown ethers has long been investigated for the radium cation extraction from environmental and nuclear waste samples. Taking advantage of the well-known size-selective properties of these chelators, the complexation of Ra^{2+} was found synergized by the 18-crown-6 (18C6) or 21-crown-7 (21C7) derivatives.[8] Since the thermodynamic constants were measured at the same time for barium, accurate constants can be deduced for the following exchange reactions:
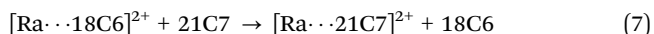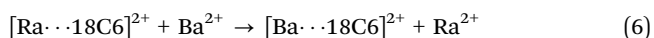
$$[Ra\cdots18C6]^{2+} + Ba^{2+} \rightarrow [Ba\cdots18C6]^{2+} + Ra^{2+} \quad (6)$$

$$[Ra\cdots18C6]^{2+} + 21C7 \rightarrow [Ra\cdots21C7]^{2+} + 18C6 \quad (7)$$

The reaction (6) was studied by following the thermodynamic cycle presented in Scheme 2, with $m = 1$ and $n = 0$ in accordance of the guidelines for use of the SMD model.[53] The computations were performed with three of the DFT methods. The reaction (7) was studied according to the thermodynamic cycle displayed on Scheme 1, with radium as the metal. The SMD model does not require adding solvent molecules ($m = n = 0$), and the computational methodology was that described along with Scheme 1. The calculated structures for the most stable conformation of $[Ba\cdots18C6]^{2+}$, $[Ra\cdots18C6]^{2+}$, and $[Ra\cdots21C7]^{2+}$ are shown in Fig. S5 in ESI,† while Table 7 presents the calculated and experimental values of $\log K_{exc}$ for reactions (6) and (7). The deviations between the calculated values are moderate, at most 0.6 on the log scale. For the metal exchange reaction (6), the mean of calculated $\log K_{exc}$ values, 0.08, almost coincides with the experimental value, 0.20 ± 0.40.[8] It is the same conclusion for the exchange between the two crown ethers: the mean of calculated $\log K_{exc}$ for reaction (7) is -0.01 while the experimental value is -0.10 ± 0.30.[8] It is therefore confirmed that the value of 2.110 Å as the Coulomb radii to use for radium in the SMD model is satisfactory.

Contribution of relativistic effects

The computational methodology that has been established seems to satisfy the targeted objective of better accuracy than 1 in log unit on the calculated equilibrium constants. Because it involves quasi-relativistic 2c-DFT calculations, a lighter version of the methodology might be desirable for the study of large radium chelators. In this perspective, the impact of limiting oneself to pseudo-relativistic calculations, *i.e.* sr-DFT, should be evaluated. The interaction of the electron spin with magnetic fields generated by other charged particles in relative motion, leading to the coupling between electron spin and orbital momentum, is often neglected in structure determination and in thermochemistry calculations. However, SOC can be for some heavy elements even more important than scalar-relativistic effects. For a given property, the SOC effect (ΔSO) is defined here as the difference between the results from 2c-DFT and sr-DFT calculations. Table 8 shows how SOC affects the structure of the radium complexes previously studied in the Geometric benchmark section.

The structures computed without considering and considering the effects of the SOC are globally close, whatever the used DFT functional. The superposition between the two types of structure, for the three studied complexes, gives values of the root-mean-square deviation (RMSD) of atomic positions that are smaller than 0.015 Å. Focusing on the geometrical

Table 6 Calculated values of $\log K_{exc}$ for the exchange reactions between Ra^{2+} and Ba^{2+}, using the SMD implicit model ($r_{Ba} = 2.045$ Å) and selected DFT functionals

		Ra Coulomb radius			
	DFT functional	2.115 Å	2.110 Å	2.105 Å	2.100 Å
$L = HO^-$ exp.[64]	ωB97X	0.19	0.26	−0.19	−0.14
	M08-HX	−0.58	−0.50	−0.43	−0.36
0.00 ± 0.40	MN15	−0.26	−0.18	−0.11	−0.04
	PW6B95	−0.16	−0.10	−0.04	0.03
$L = EDTA^{4-}$ exp.[63]	ωB97X	0.56	0.85	1.14	1.43
	M08-HX	0.51	0.81	1.12	1.42
0.73 ± 0.16	MN15	0.37	0.68	0.98	1.28
	PW6B95	0.86	1.15	1.45	1.75
WMAE		0.27	0.23	0.28	0.36

Table 7 Calculated values of $\log K_{exc}$ for the exchange reactions (6) and (7), using the SMD implicit model ($r_{Ba} = 2.045$ Å, $r_{Ra} = 2.110$ Å) and selected DFT functionals

	Reaction (6)	Reaction (7)
exp.	0.20 ± 0.40[8]	-0.10 ± 0.30[8]
ωB97X	0.17	−0.08
M08-HX	0.31	0.31
MN15	−0.26	−0.27

Table 8 SOC effect at the DFT/ACVDZ level of theory on interaction distances in Ra^{2+} complexes with CO_3^{2-}, SO_4^{2-} and H_2O

			Ra–O distance (Å)		
	DFT functional	RMSD (Å)	sr	2c	ΔSO
$RaCO_3$	ωB97X	0.008	2.419	2.400	−0.019
	MN15	0.008	2.404	2.384	−0.020
$RaSO_4$	ωB97X	0.012	2.619	2.594	−0.025
	MN15	0.010	2.596	2.574	−0.022
RaH_2O	ωB97X	0.013	2.708	2.677	−0.031
	MN15	0.014	2.697	2.663	−0.034

parameters of the interaction between radium and the three ligands, it is found that the SOC systematically reduces the interaction distances. The magnitude of this decrease appears to be related to the strength of the interaction. The larger the interaction distance, the larger the decrease with SOC. However, the geometrical modification remains limited: ΔSO is for example always smaller than 1.1% with the ωB97X functional. It is worth recalling that for these same complexes, the inaccuracy on computed interaction distances at the sr-ωB97X/ACVDZ level of theory was previously estimated to be 1.3% (*cf.* Table 2). SOC effect is thus of the same order of magnitude as the uncertainty on the computed geometries, which justifies here the approach of not considering this relativistic effect in the geometry optimization calculations.

The influence of the SOC on the calculated equilibrium constants has also been evaluated. For this purpose, the three metal exchange reactions between Ra^{2+} and Ba^{2+} have been reinvestigated by substituting in the previous computational methodology the 2c-DFT calculations by sr-DFT calculations. Table 9 presents the SOC effect on the calculated values of $\log K_{exc}$. For each studied reaction, the negative value of ΔSO indicates a shift of the equilibrium towards the Ra(II) complex. The interaction of radium with its ligands appears significantly strengthened, which is consistent with the previous finding of decreased interaction distances with SOC (*cf.* Table 8). The study of the competition between Ra^{2+} and Ba^{2+} cations, by evaluating the selectivity of a ligand, obviously requires considering the relativistic spin–orbit interaction in view of the ΔSO magnitude, from 0.4 to 1.0 in log unit. Moreover, the scalar-relativistic values of $\log K_{exc}$ are not accurate. With the ωB97X functional and for L = HO^-, the deviation from the experimental value is 3 times larger than that between the two-component relativistic value and the experimental value. For L = $EDTA^{4-}$, it

is 7 times larger, and 13 times larger for L = 18C6. It can also be said for the exchange reaction with $EDTA^{4-}$, that the deviation determined for the sr-ωB97X value (0.84) is even larger than the experimental value of $\log K_{exc}$ (0.73). The SOC effect on the stability of Ra(II) complexes can definitely not be neglected.

Application to targeted alpha therapy

So far, it has been established a cost-effective computational methodology that is reliable for investigating the coordination and complexation chemistry of radium in solution. As a straightforward application, we have reassessed the potency of the only chelator identified to date as suitable for biomedical applications. Macropa is a diaza-18-crown-6 core macrocyclic with two pendent picolinate donor arms. N. A. Thiele and coworkers have previously shown that its deprotonated form macropa^{2-} forms a complex of high thermodynamic stability with Ba^{2+},[65] prompting its recent investigation as a chelator for the bigger Ra^{2+} ion.[13] The most significant outcome is that the Ra^{2+} chelation utilizing a bifunctional derivative of macropa conjugated to a single amino acid, β-alanine, was found stable under biological conditions. Except the *in vivo* stability of the [^{223}Ra]Ra(macropa) complex, no quantitative data on the interaction between macropa and Ra^{2+} was presented at that time. Such data are essential to allow comparison to other ligands, and to locate them on an affinity scale. Quantitative data are also essential to characterize the selectivity of a ligand with respect to, for example, alkaline-earth ions Ca^{2+} and Mg^{2+} that are present in the biological medium.

The presented computational methodology can make up for the tough experimental investigations of this radioelement, providing numerical information to help in the rational design of efficient chelators for biomedical applications. An accurate estimate of the selectivity of macropa between the Ra^{2+} and Ba^{2+} ions can be calculated according to the thermodynamic cycle shown in Scheme 2, with L = macropa^{2-}. The ωB97X, M08-HX and MN15 functionals have been used, the DFT computations being performed following the methodology described along with Scheme 2. The alkaline-earth cations were clustered with one water molecule, $m = 1$, while n was varied by up to 3 for the macropa complexes. Beginning with $n = 0$, several geometrical conformations could be optimized for the macropa complexes. Interestingly, the most stable conformation is found to be the
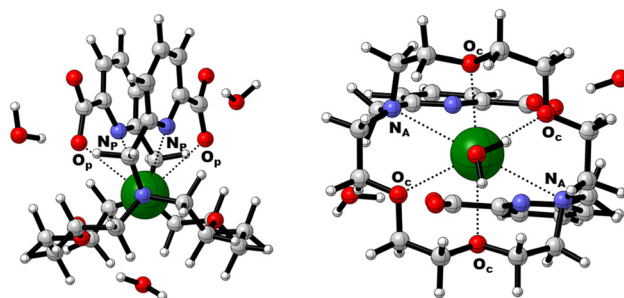
Table 9 SOC effect on the equilibrium constant of exchange reactions between Ra^{2+} and Ba^{2+}

		$\log K_{exc}$		
	DFT functional	sr	2c	ΔSO
L = HO^-	ωB97X	0.86	0.26	−0.60
exp. 0.00 ± 0.40[64]	MN15	0.52	−0.18	−0.71
L = $EDTA^{4-}$	ωB97X	1.57	0.85	−0.72
exp. 0.73 ± 0.16[63]	MN15	1.67	0.68	−1.00
L = 18C6	ωB97X	0.58	0.17	−0.41
exp. 0.20 ± 0.40[8]	MN15	0.28	−0.26	−0.54

Fig. 3 Side and bottom views of the most stable conformation of [Ra(macropa)(H$_2$O)$_3$] at the SMD sr-MN15/ACVDZ level of theory. N$_P$ = pyridyl nitrogen atoms, O$_P$ = picolinate oxygen atoms, O$_C$ = crown oxygen atoms, N$_A$ = amine nitrogen.

Table 10 Calculated values of $\log K_{exc}$ for the reaction (8), using n and $m = 1$ water molecules for micro-solvation and selected DFT functionals

	DFT functional			
	ωB97X	M08-HX	MN15	Average
$n = 0$	2.04	0.76	0.01	0.93
$n = 1$	1.68	2.59	2.01	2.09
$n = 3$	2.05	2.43	2.03	2.17

same for radium and barium. Moreover, the computed structure for Ba^{2+} is very close to the X-ray structure of the cation $[Ba(Hmacropa)]^+$ previously crystallized *via* vapor diffusion of Et_2O into a DMF solution.[65] For instance, the interaction distances calculated at the SMD sr-MN15/ACVDZ level of theory between Ba^{2+} and the donor atoms of macropa^{2-} differ on average by 0.7% from the crystallographic distances (see Table S6 in ESI†).

According to the guidelines for use of the SMD model (case of oxygen atoms bearing a partial atomic charge more negative than the charge on oxygen in water),[53] water molecules were then added to the complexes in order to neutralize the charged oxygen atoms of the picolinate arms that do not interact with the metal cation. An additional water molecule was added to complete the coordination sphere of the metal, similar to the way DMF completes the coordination sphere of barium in the crystallographic structure of $[Ba(Hmacropa)]^+$.[65] With $n = 3$, the computed structure at the SMD sr-MN15/ACVDZ level of theory is shown in Fig. 3 for the most stable conformation Ra(macropa). The coordination sphere of Ra^{2+} comprises all 10 donor atoms (N_4O_6) of macropa^{2-}. The interaction distances are lengthened compared to those computed for the same conformation of Ba(macropa), on average by 0.05 Å (Table S6, ESI†).

Before experimental results are reported, the equilibrium constant was determined for the metal exchange reaction (8) using the ωB97X, M08-HX and MN15 functionals:[26]

$$Ra(macropa) + Ba^{2+} \rightarrow Ba(macropa) + Ra^{2+} \qquad (8)$$
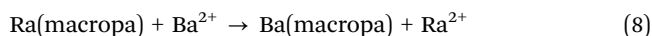
Although macropa showed a tendency for binding to large over small ions, which was confirmed for alkaline-earth ions up to barium,[65] the results for radium establish a divergence for the larger ions. Indeed, the affinity of deprotonated macropa^{2-} for Ra^{2+} was determined significantly weaker than that for Ba^{2+}.[26] The calculated values of the equilibrium constant, with n varied by up to 3, are presented in Table 10. According to the number of water molecules used to cluster the Ra(II) and Ba(II) complexes, the mean value of $\log K_{exc}$ varies between 0.9 and 2.1, *i.e.* the Ba(II) complex is predicted between one and two orders of magnitude stronger. This outcome is corroborated by the very recent experimental study of the competition between Ra^{2+} and Ba^{2+}.[27] N. A. Thiele and co-workers report that "unexpectedly, macropa complex stability drops by nearly $1.5 \log K$ units on moving from the large Ba^{2+} ion to the even larger Ra^{2+} ion". Thanks to molecular modeling tools, we can not only predict that macropa is a notably less suitable chelator for radium than barium, in contrast to the trend inferred from supposedly non-radioactive analogues,[65] but we can also provide quantitative data.

Conclusions

The lack of insight into the chemistry of metallic radioelements experimentally studied at ultra-trace concentrations prevents the optimization of specific chelators. A strategy is presented to establish a computational methodology that is fast, flexible, and sufficiently accurate for a given radiometal to supplement the available experimental data on its coordination properties. The computational methodology involves quantum mechanical methods. It must notably allow to simulate the influence of a solvent and also to treat the relativistic effects for the heaviest radiometals. This strategy is applied to the emblematic case of radium, whose $[^{223}Ra]Ra^{2+}$ cation as a chloride salt is the first and currently the only alpha-emitting drug authorized for cancer therapy.

A selection among 15 popular or recent DFT methods is first performed, guided by comparisons with structures and interaction energies obtained on small-size Ra-species using the gold standard CCSD(T) method. The ωB97X, M08-HX, MN15 and PW6B95 functionals represent the best compromise when energies are computed using basis sets of triple-zeta quality on geometries previously optimized using basis sets of double-zeta quality. Then the question of solvent effects is addressed. Implicit models can be said universal and accurate, but they heavily rely on empirical parameters used for the construction of the solute cavity. Some of the few constants measured for Ra^{2+} complexation, combined through isodesmic-like reactions in order to benefit from error cancellation mechanisms, allowed a radium-specific cavity to be fitted within the SMD solvation model. Regarding the relativistic effects on calculated equilibrium constants, the latter can be deteriorated by one order of magnitude if the relativistic spin–orbit interaction is neglected. Indeed, the multiple interactions of Ra(II) with donor atoms lead to partial occupancy of orbitals with non-zero angular-momentum quantum numbers l, which are particularly sensitive to spin–orbit coupling for this heavy radioelement ($Z = 88$). Although still neglected in recent studies,[66] these relativistic characteristics of radium impact on the interaction energies and stabilities of the resulting Ra(II) complexes.

In the end, the precision of the established methodology on Ra^{2+} complexation constants is 1 in log unit. It allows for a series of potential ligands to accurately quantify their affinities for this radiometal cation, or to evaluate the selectivity of a ligand towards other cations present in the considered conditions. The benefits of molecular modeling to help in the rational design of efficient chelators is shown with macropa, a macrocyclic ligand used recently for coupling Ra^{2+} to biological targeting vectors.[13] The rationale is that macropa forms with Ba^{2+} a complex of high thermodynamic stability, and Ra(II) is supposed to show coordination properties similar to those of Ba(II). However, the assumption that macropa might be as suitable for binding to Ra^{2+} is challenged by molecular modeling. The Ra(II) complex is calculated to be about 2 orders of magnitude weaker than the Ba(II) complex, in agreement with very recent solid-state results showing that Ra^{2+} coordination chemistry cannot always be predicted using Ba^{2+}.[67]

Conflicts of interest

Acknowledgements

References

1 N. Guo, R. Maurice, D. Teze, J. Graton, J. Champion, G. Montavon and N. Galland, *Nat. Chem.*, 2018, **10**, 428–434.

2 L. Liu, S. Rahali, R. Maurice, C. G. Pech, G. Montavon, J.-Y. L. Questel, J. Graton, J. Champion and N. Galland, *Chem. Sci.*, 2021, **12**, 10855–10861.

3 J. Champion, C. Alliot, E. Renault, B. M. Mokili, M. Chérel, N. Galland and G. Montavon, *J. Phys. Chem. A*, 2010, **114**, 576–582.

4 D.-C. Sergentu, D. Teze, A. Sabatié-Gogova, C. Alliot, N. Guo, F. Bassal, I. D. Silva, D. Deniaud, R. Maurice, J. Champion, N. Galland and G. Montavon, *Chem. – Eur. J.*, 2016, **22**, 2964–2971.

5 A. Stoïanov, J. Champion and R. Maurice, *Inorg. Chem.*, 2019, **58**, 7036–7043.

6 E. Acher, M. Masella, V. Vallet and F. Réal, *Phys. Chem. Chem. Phys.*, 2020, **22**, 2343–2350.

7 P. L. Brown, A. V. Matyskin and C. Ekberg, *Radiochim. Acta*, 2022, **110**, 505–513.

8 M. L. Dietz, R. Chiarizia, E. P. Horwitz, R. A. Bartsch and V. Talanov, *Anal. Chem.*, 1997, **69**, 3028–3037.

9 C. W. Sill, *Nucl. Chem. Waste Manage.*, 1987, **7**, 239–256.

10 International Atomic Energy Agency, *The Environmental Behaviour of Radium: Revised Edition*, Technical Reports Series No. 476, IAEA, Vienna, 2014.

11 M. Boudias, A. Gourgiotis, G. Montavon, C. Cazala, V. Pichon and N. Delaunay, *J. Environ. Radioact.*, 2022, **244–245**, 106812.

12 P. G. Kluetz, W. Pierce, V. E. Maher, H. Zhang, S. Tang, P. Song, Q. Liu, M. T. Haber, E. E. Leutzinger, A. Al-Hakim, W. Chen, T. Palmby, E. Alebachew, R. Sridhara, A. Ibrahim, R. Justice and R. Pazdur, *Clin. Cancer Res.*, 2014, **20**, 9–14.

13 D. S. Abou, N. A. Thiele, N. T. Gutsche, A. Villmer, H. Zhang, J. J. Woods, K. E. Baidoo, F. E. Escorcia, J. J. Wilson and D. L. J. Thorek, *Chem. Sci.*, 2021, **12**, 3733–3742.

14 E. W. Price and C. Orvig, *Chem. Soc. Rev.*, 2013, **43**, 260–290.

15 D. Sneddon and B. Cornelissen, *Curr. Opin. Chem. Biol.*, 2021, **63**, 152–162.

16 D. Langmuir and A. C. Riese, *Geochim. Cosmochim. Acta*, 1985, **49**, 1593–1601.

17 P. L. Brown, A. V. Matyskin and C. Ekberg, *Radiochim. Acta*, 2022, **110**, 505–513.

18 J. Kleynhans, H. G. Kruger, T. Cloete, J. R. Zeevaart and T. Ebenhan, *Curr. Med. Chem.*, 2020, **27**, 7048–7063.

19 M. Salahinejad, D. A. Winkler and F. Shiri, *Curr. Radiopharm.*, 2022, **15**, 271–319.

20 E. Y. Lau, F. C. Lightstone and M. E. Colvin, *Inorg. Chem.*, 2006, **45**, 9225–9232.

21 F. Y. Adeowo, B. Honarparvar and A. A. Skelton, *J. Phys. Chem. A*, 2017, **121**, 6054–6062.

22 A. Morgenstern, L. M. Lilley, B. W. Stein, S. A. Kozimor, E. R. Batista and P. Yang, *Inorg. Chem.*, 2021, **60**, 623–632.

23 A. Matsuda and H. Mori, *J. Comput. Chem. Jpn.*, 2014, **13**, 105–113.

24 A. Matsuda and H. Mori, *J. Solution Chem.*, 2014, **43**, 1669–1675.

25 A. V. Matyskin, R. Ylmen, P. Lagerkvist, H. Ramebäck and C. Ekberg, *J. Solid State Chem.*, 2017, **253**, 15–20.

26 H. Mohaman, G. Montavon and N. Galland, *Nucl. Med. Biol.*, 2022, **108–109**, S154–S155.

27 A. S. Ivanov, M. E. Simms, V. S. Bryantsev, P. D. Benny, J. R. Griswold, L. H. Delmau and N. A. Thiele, *Chem. Commun.*, 2022, **58**, 9938–9941.

28 T. Saue, *ChemPhysChem*, 2011, **12**, 3077–3094.

29 I. S. Lim, H. Stoll and P. Schwerdtfeger, *J. Chem. Phys.*, 2006, **124**, 034107.

30 M. J. Frisch, G. W. Trucks, H. B. Schlegel, G. E. Scuseria, M. A. Robb, J. R. Cheeseman, G. Scalmani, V. Barone, G. A. Petersson, H. Nakatsuji, X. Li, M. Caricato, A. V. Marenich, J. Bloino, B. G. Janesko, R. Gomperts, B. Mennucci, H. P. Hratchian, J. V. Ortiz, A. F. Izmaylov, J. L. Sonnenberg, Williams, F. Ding, F. Lipparini, F. Egidi, J. Goings, B. Peng, A. Petrone, T. Henderson, D. Ranasinghe, V. G. Zakrzewski, J. Gao, N. Rega, G. Zheng, W. Liang, M. Hada, M. Ehara, K. Toyota, R. Fukuda, J. Hasegawa, M. Ishida, T. Nakajima, Y. Honda, O. Kitao, H. Nakai, T. Vreven, K. Throssell, J. A. Montgomery Jr., J. E. Peralta, F. Ogliaro, M. J. Bearpark, J. J. Heyd, E. N. Brothers, K. N. Kudin, V. N. Staroverov, T. A. Keith, R. Kobayashi, J. Normand, K. Raghavachari, A. P. Rendell, J. C. Burant, S. S. Iyengar, J. Tomasi, M. Cossi, J. M. Millam, M. Klene, C. Adamo, R. Cammi, J. W. Ochterski, R. L. Martin, K. Morokuma, O. Farkas, J. B. Foresman and D. J. Fox, *Gaussian 16 Rev. A.03*, 2016.

31 P. J. Stephens, F. J. Devlin, C. F. Chabalowski and M. J. Frisch, *J. Phys. Chem.*, 1994, **98**, 11623–11627.

32 A. D. Becke, *J. Chem. Phys.*, 1993, **98**, 5648–5652.

33 C. Adamo and V. Barone, *J. Chem. Phys.*, 1998, **108**, 664–675.

34 C. Adamo and V. Barone, *J. Chem. Phys.*, 1999, **110**, 6158–6170.

35 H. L. Schmider and A. D. Becke, *J. Chem. Phys.*, 1998, **108**, 9624–9631.

36 V. N. Staroverov, G. E. Scuseria, J. Tao and J. P. Perdew, *J. Chem. Phys.*, 2003, **119**, 12129–12137.

37 A. D. Boese and N. C. Handy, *J. Chem. Phys.*, 2002, **116**, 9559–9569.

38 A. D. Boese and J. M. L. Martin, *J. Chem. Phys.*, 2004, **121**, 3405–3416.

39 Y. Zhao and D. G. Truhlar, *J. Phys. Chem. A*, 2005, **109**, 5656–5667.

40 Y. Zhao and D. G. Truhlar, *Theor. Chem. Acc.*, 2008, **120**, 215–241.

41 Y. Zhao and D. G. Truhlar, *J. Chem. Theory Comput.*, 2008, **4**, 1849–1868.

42 H. S. Yu, X. He, S. L. Li and D. G. Truhlar, *Chem. Sci.*, 2016, **7**, 5032–5051.

43 J. Heyd, G. E. Scuseria and M. Ernzerhof, *J. Chem. Phys.*, 2003, **118**, 8207–8215.

44 A. V. Krukau, O. A. Vydrov, A. F. Izmaylov and G. E. Scuseria, *J. Chem. Phys.*, 2006, **125**, 224106.

45 J.-D. Chai and M. Head-Gordon, *J. Chem. Phys.*, 2008, **128**, 084106.

46 J. G. Hill and K. A. Peterson, *J. Chem. Phys.*, 2017, **147**, 244106.

47 T. H. Dunning, *J. Chem. Phys.*, 1989, **90**, 1007–1023.

48 R. A. Kendall, T. H. Dunning and R. J. Harrison, *J. Chem. Phys.*, 1992, **96**, 6796–6806.

49 D. E. Woon and T. H. Dunning, *J. Chem. Phys.*, 1993, **98**, 1358–1371.

50 C. J. Cramer, *Essentials of Computational Chemistry: Theories and Models*, John Wiley & Sons, Chichester, England, Second edn, 2013.

51 D. Feller, *J. Chem. Phys.*, 1992, **96**, 6104–6114.

52 F. N. N. Pansini, A. C. Neto and A. J. C. Varandas, *Chem. Phys. Lett.*, 2015, **641**, 90–96.

53 A. V. Marenich, C. J. Cramer and D. G. Truhlar, *J. Phys. Chem. B*, 2009, **113**, 6378–6396.

54 C. R. Groom, I. J. Bruno, M. P. Lightfoot and S. C. Ward, *Acta Crystallogr., Sect. B: Struct. Sci., Cryst. Eng. Mater.*, 2016, **72**, 171–179.

55 Y. Marcus, *Ions in Solution and their Solvation*, Wiley, Hoboken, NJ, 1st edition., 2015.

56 W. R. Fawcett, *J. Phys. Chem. B*, 1999, **103**, 11181–11185.

57 N. M. Bazhin, *J. Phys. Chem. A*, 2020, **124**, 11051–11060.

58 M. D. Tissandier, K. A. Cowen, W. Y. Feng, E. Gundlach, M. H. Cohen, A. D. Earhart, J. V. Coe and T. R. Tuttle, *J. Phys. Chem. A*, 1998, **102**, 7787–7794.

59 V. S. Bryantsev, M. S. Diallo and W. A. Goddard III, *J. Phys. Chem. B*, 2008, **112**, 9709–9719.

60 T. Sekine, M. Sakairi and Y. Hasegawa, *Bull. Chem. Soc. Jpn.*, 1966, **39**, 2141–2144.

61 S. Capone, A. De Robertis, C. De Stefano and R. Scarcella, *Talanta*, 1985, **32**, 675–677.

62 R. M. Noyes, *J. Am. Chem. Soc.*, 1962, **84**, 513–522.

63 A. V. Matyskin, N. L. Hansson, P. L. Brown and C. Ekberg, *J. Solution Chem.*, 2017, **46**, 1951–1969.

64 A. V. Matyskin, P. L. Brown and C. Ekberg, *J. Chem. Thermodyn.*, 2019, **128**, 362–371.

65 N. A. Thiele, S. N. MacMillan and J. J. Wilson, *J. Am. Chem. Soc.*, 2018, **140**, 17071–17078.

66 Z. Bai, J. Brannon, C. Celis-Barros, N. Beck, J. M. Sperling, B. M. Rotermund, D. G. Martinez, H. B. Wineinger and T. E. Albrecht-Schönzart, *Inorg. Chem.*, 2023, **62**, 8478–8481.

67 F. White, N. Thiele, M. Simms and S. Cary, *ChemRxiv*, 2023, preprint, DOI: **10.26434/chemrxiv-2023-lx8c1**.